Fuel 407 (2026) 137277

Contents lists available at ScienceDirect

Fuel

journal homepage: www.elsevier.com/locate/jfue

Full length article

Combustion of a single iron-based impure particle: numerical analysis of four non-volatile oxide impurities using a parametric approach

Z. Bruyr [a,*], L. Choisez [a], L.C. Thijs [b], X.C. Mi [b,c], P.J. Jacques [a], F. Halter [d], F. Contino [a]

[a] Institute of Mechanics, Materials and Civil Engineering (iMMC), Université catholique de Louvain (UCLouvain), Place du Levant, 2, 1348, Louvain-la-Neuve, Belgium
[b] Department of Mechanical Engineering, Eindhoven University of Technology, P.O. Box 513, NL-5600 MB, Eindhoven, the Netherlands
[c] Eindhoven Institute of Renewable Energy Systems, Eindhoven University of Technology, NL-5600 MB, Eindhoven, the Netherlands
[d] CNRS – ICARE, University Orléans, F-45072 Orléans, France

HIGHLIGHTS

- Iron powders containing non-volatile impurities show a promising potential for use as high-energy dense carriers.
- A parametric approach allows highlighting the impact of each impurity’s properties and phenomena on the combustion process.
- Non-volatile impurities with a high specific heat capacity and latent heat of melting reduce the peak temperature, nanoparticle production and NOx emissions.
- The creation of a complex ternary oxide due to liquid-state interactions might prevent a full energy release and the powder recyclability.

ARTICLE INFO

Keywords:
Metal fuels
Iron combustion
Impurities
Single particle
Alloy design

ABSTRACT

Iron powder has been proposed as a high energy-dense, sustainable, safe and abundant energy carrier. However, despite a rising number of studies related to pure iron combustion, the influence of impurities on the combustion is still unclear. The objective of the current study is to understand how the presence of a non-volatile oxide impurity at a varying concentrations impacts the peak temperature and combustion time. To this end, we developed a single-particle combustion model containing up to 20 wt.% of Al_2O_3, SiO_2, MnO or CaO. The combustion regime is assumed to be fully external-diffusion-limited and the oxidation is limited to stoichiometric FeO ($X_O = 0.5$ in the liquid phase). The model predicts a decrease in peak temperature (up to 146 K with 20 wt.% of MnO), in liquid combustion time (up to 11.5 % with 20 wt.% of SiO_2) and in the time to peak temperature (up to 23 % with 20 wt.% of SiO_2). Both phenomena limit nanoparticle formation and micro-explosion event frequency, two of the main issues currently faced in pure Fe combustion. Iron combustion is already a low NO emissions process, which can also be further reduced with the addition of non-volatile impurities. The possibility of creating a complex ternary oxide phase is investigated and the challenges of incomplete oxidation or reduction are discussed. The assumptions made in the numerical model are questioned and the effect of impurities on them is discussed. This work highlights the promising potential of the presence of non-volatile impurities in Fe powders for their use as high-energy dense carriers. Most promising compositions will be selected based on this model and experimentally tested to validate the numerical results and improve the single-particle model in a future work.

1. Introduction

Renewable energy production capacity is growing worldwide to substitute the use of fossil fuels [1]. However, their intermittent nature in time and space requires clean and sustainable energy carriers [2]. Among the different energy storage technologies, metal-fuels have recently emerged as promising highly-dense energy carriers [3]. Iron powder in particular is considered for this application due to its carbon-free, recyclable, safe, cheap, and abundant nature [3].

Iron ores and recycled steels are not pure; they contain different impurities. Besides, their composition varies considerably from one source to another. Choisez et al. [4] present an overview of the impurity content found in numerous iron sources. Most impurities present in iron ores are in the oxide form and with a concentration of up to 34 wt.%. In

---

[*] Corresponding author.
Email address: zakarie.bruyr@uclouvain.be (Z. Bruyr).

https://doi.org/10.1016/j.fuel.2025.137277
Received 10 January 2025; Received in revised form 8 September 2025; Accepted 19 October 2025

particular, SiO_2, Al_2O_3, CaO and MnO are often found in Fe-rich ores: Among 73 sources of iron ores with at least 50 wt.% of Fe, 96 % contain SiO_2 and Al_2O_3 with a concentration of up to 34 wt.%. CaO and MnO are present respectively in 60 % and 53 % of the sources with a concentration varying between 0.01 wt.% and 12 wt.%.

Impurities behave differently depending on their form (i.e. metallic or oxide). During the combustion process, metallic impurities are oxidized and might partially or completely evaporate [4]: 5 wt.% of sulfur, carbon, molybdenum, copper or phosphorus inside a pure Fe powder evaporates between 20 wt.% and 100 wt.%. This type of impurity is called 'volatile'. Gasification of volatile impurities has been suggested as a potential origin of micro-explosions occurring during iron particle combustion [5–7]. In contrast, evaporation of metal oxide impurities during iron combustion is limited (lower than 1 wt.% [4]). This second type of impurity is called 'non-volatile'. Mostly various metal oxides are concerned but some metallic impurities are also included, such as aluminum, silicon or titanium. However, once they get oxidized, they remain in the oxide form throughout the consecutive combustion-reduction cycles.

Despite a rising number of publications related to the use of pure iron powder, only two papers have tackled the important question of the influence of impurities on the combustion process. The combustion of Si-containing iron powders was experimentally characterized by Peng et al. [8]. A lower peak temperature was reached compared to pure iron as well as less oxidized combustion products. Choisez et al. [4] used thermodynamic simulations to predict the variation of flame temperature, iron and impurity evaporation and oxygen gas release upon solidification for a system containing 5 wt.% of impurity compared to pure iron. The addition of non-volatile oxide impurities is expected to decrease the flame temperature, evaporation, and also the energy density.

Numerical models for the combustion of a single pure iron particle are continuously improved. First, Soo et al. [9] developed a generic combustion model for ideal non-volatile fuel particles controlled by both the oxygen diffusion rate to the particle surface and the surface kinetics. They determined that there is a transition, called ignition, from a kinetics-limited combustion regime to a diffusion-limited. To better predict the transition temperature, Mi et al. [10] constructed an ignition model for pure iron using solid-phase oxidation kinetics described by a parabolic rate. Their results predict an ignition temperature of approximately 1080 K for a pure iron particle with a diameter above 5 μm in air. The combustion of ignited particles can then be limited by three potential mechanisms: (i) oxygen diffusion to the particle surface, (ii) oxygen surface chemisorption, and (iii) ions' internal transport. Thijs et al. [11] developed a boundary layer resolved model including Stefan flow, evaporation and solidification of the evaporated iron (oxide) in nano-oxide particles, and temperature-dependent properties. This model only considers oxidation from Fe to FeO, fully achieved at the maximum temperature, and neglects surface chemisorption and internal transport. A good agreement was still obtained with the single-particle experimental data of Ning et al. [12,13] for the combustion time and maximum temperature at ambient oxygen concentration. This model was then used by Thijs et al. [14] to improve a Lagrangian point particle model also achieving a reasonable match with the same experimental results while reducing the computational costs. They still assume a combustion regime fully limited by the external diffusion of oxygen and oxidation limited to stoichiometric FeO ($X_O = 0.5$ in the liquid phase). However, the initial heating rate, the peak temperature and the cooling rate were still overestimated.

First, Thijs et al. [15] extended the previous model [14] to include oxygen surface chemisorption using molecular dynamics simulations and showed that it can reduce the heating rate during the initial phase before reaching the maximum particle temperature. Second, Fujinawa et al. [16] and Thijs et al. [17] showed that ion internal transport plays a role in limiting the peak temperature. Finally, oxidation beyond FeO has been investigated by Mich et al. [18] using equilibrium calculations. They better predicted the temperature profile during reactive cooling by defining an oxidation limit when the oxygen vapor pressure at the particle surface approaches that of the bulk gas. Among the mentioned models, the boundary layer resolved model of Thijs et al. [11] includes nanoparticle formation assuming that gaseous iron atoms oxidize first to $FeO_2(g)$ rapidly followed by a conversion to solid Fe_2O_3, namely the confirmed composition of nanoparticles outside of the combustion chamber [19]. However, the nanoparticle composition in the boundary layer during combustion may rather correspond to FeO above 2000 K as shown by Li et al. [20]. Nguyen et al. [21] therefore developed an extension of the boundary layer resolved model by including liquid FeO at the onset of nanoparticle formation. Their results indicate that the particle temperature plays an essential role and they achieved a total mass loss between 6 and 12 wt.% for particle diameters between 60 μm and 40 μm, respectively.

Several experimental results obtained from pure iron combustion highlighted the presence of nanoparticles [7,19,22–24]. This unwanted phenomenon suggests that iron evaporation occurs even though temperature does not exceed the boiling point of liquid iron (3140 K) and liquid iron oxide (3396 K). Oxidation of evaporated iron leads to nanoparticle production. The amount of iron evaporated has been quantified by Wiinikka et al. [25] to 4 wt.%, by Poletaev and Khlebnikova [6] predicting 15 % to 20 % of combustion product loss due to evaporation, by Prasidha et al. [26] to between 0.01 and 0.13 wt.%, and several other studies [27–29] between 1.2 and 7.4 wt.% of iron evaporated or mass losses. This shows the remaining high uncertainty about the exact amount of iron evaporated during the combustion. Also, Ning et al. [30] observed that the critical temperature for nanoparticle cloud formation during the combustion of iron particles with an average diameter of 49.3 μm is 2100 K and that the evaporation mostly comes from the evaporation of pure liquid iron.

Another unwanted but observed phenomenon is the occurrence of micro-explosions [5–7,13,31]. It consists of the breakup of melted iron particles into smaller burning pieces, affecting the size, microstructure and shape of the burned particles. Accordingly, this may considerably affect the recyclability of the powder by decreasing the collection efficiency and preventing a proper reduction. It has been suggested that this phenomenon arises from internal boiling inducing a too high pressure difference with the surroundings, especially near the peak temperature [5,23,31]. Possible sources of gas are either dissolved gases like N2 or O2, or the vaporization of metal or metal oxides inside the burning particles [5]. The presence of volatile impurities such as carbon is therefore suspected to increase micro-explosion frequency. Yet, the exact origin of the micro-explosion is not yet fully understood.

The particle temperature achieved during the combustion exceeds the temperature at which NO production starts (around 1800 K). The presence of nitrogen and oxygen above that temperature and for sufficient residence time (above 5 ms) leads to thermal NO [32]. However, due to the absence of N and CH inside iron particles, only the thermal Zeldovich mechanism can produce NO emissions. Therefore, iron combustion technology is often described as a low-NOx technology [25,33].

The cyclic character of the MeCRE has been proven experimentally with pure iron. Baigmohammadi et al. [34] succeeded in burning the same powder in up to two cycles of combustion-reduction without significant differences. Stevens et al. [35] also succeeded in performing 3 combustion-reduction cycles under the same conditions with a stable particle size distribution although it required additional intermediate treatments, such as grinding and sieving.

The paper is structured as follows: Section 2 describes how the modified properties and induced phenomena due to the presence of non-volatile impurities are incorporated into the numerical model using a parametric approach. Section 3 presents the predicted influence of oxide impurities on the peak temperature, characteristic combustion time scales, evaporation, NO emissions, energy density, and reduction. Finally, a conclusion concludes the paper in Section 4. This paper constitutes a foundational basis for future similar studies on other impurities and opens doors for a study of fine-tuning an alloy that could improve the combustion and reduction of the powder used in the MeCRE. Similar to other well-developed combustion technologies like coal, wood, or internal combustion engines, this fuel-design approach is complementary to other approaches intended to improve the combustion process such as optimizing burner design, tuning the operating conditions, and post-treating the emissions and combustion products.

2. Methods

2.1. Impurity concentrations

This study focuses on the influence of the four most prevalent non-volatile oxide impurities in iron ores both in frequency and concentration: Al_2O_3, SiO_2, CaO and MnO. For the following, the generic notation 'MOx' is used to refer to these oxides. As demonstrated in supplementary material SM1, an upper limit of 20 wt.% for the impurity concentration is considered. For each oxide impurity, the most oxidized form of the element is considered as long as it is stable in both solid and liquid phases. For aluminum, silicon, and calcium the existing highest oxidation states (Al_2O_3, SiO_2 and CaO) are stable in both solid and liquid phases. However, although manganese has several oxidation states higher than MnO (such as Mn_3O_4, Mn_2O_3, or MnO_2), it is here limited to MnO due to the instability of these higher oxides in the liquid state [36].

2.2. Numerical model

We extended the improved 0D Lagrangian point particle combustion model developed by Thijs et al. [14]. For more details the readers are referred to Ref. [14]. This model predicts with reasonable accuracy the peak temperature and the time to reach it for a pure iron particle burning in ambient conditions (21 vol.% O_2 and 300 K). The ignition phase is not included and the initial temperature is considered to be 1100 K, close to the ignition temperature of 1080 K for a pure iron isolated particle larger than 5 μm in diameter burning in air [10].

Similar to the previous work [14], the model considers a 1/2-film temperature, temperature- and composition-dependent properties, Stefan flow, slip velocity, and convection, radiation and evaporation heat losses. The film temperature is used to compute gaseous properties, which are used to determine oxygen diffusion rate to the particle surface and evaporation, while accounting for the temperature difference between the particle and the surrounding gas. Properties computed at the film temperature are denoted with the subscript $_\mathrm{f}$. In this model, only the first state of oxidation (wüstite FeO in solid state) is considered. This oxidation releases 4871 $\mathrm{kJ/kg_{Fe}}$, representing 66 % of the total energy released for a complete oxidation (hematite Fe_2O_3). In the liquid state, the oxide product of liquid iron is approximated as liquid-phase FeO, i.e., with a molar ratio of oxygen of $X_\mathrm{O} = 0.5$.

The model assumes a fully external-diffusion-limited combustion regime. Therefore, oxygen diffusion from the surrounding gas to the particle surface is the only rate-limiting mechanism, assuming that oxygen surface chemisorption and ion internal transport are infinitely fast. The influence of impurities on this assumption is discussed in Section 3.5. Mass transfer equations due to the oxidation intake and evaporation are given as:

$$\frac{\mathrm{d}m_\mathrm{p}}{\mathrm{d}t} = \dot{m}_{\mathrm{O}_2}\mathrm{Da}^* - \sum_i \frac{\mathrm{d}m_{\mathrm{evap},i}}{\mathrm{d}t}, \tag{1}$$

$$\frac{\mathrm{d}m_\mathrm{Fe}}{\mathrm{d}t} = -\frac{1}{s}\dot{m}_{\mathrm{O}_2}\mathrm{Da}^* - \frac{\mathrm{d}m_\mathrm{evap,Fe}}{\mathrm{d}t}, \tag{2}$$

$$\frac{\mathrm{d}m_\mathrm{MOx}}{\mathrm{d}t} = -\frac{\mathrm{d}m_\mathrm{evap,MOx}}{\mathrm{d}t}, \tag{3}$$

with m_p the particle mass, $\dot{m}_{\mathrm{O}_2}$ the oxygen mass flux to the particle surface, Da^* the normalized Damköhler number (defined in Ref. [37]), $m_{\mathrm{evap},i}$ the evaporated mass of species i, m_Fe the mass of unburned iron inside the particle and s the stoichiometric mass ratio. As oxidation is here limited to FeO, $s = \frac{1}{2}M_{\mathrm{O}_2}/M_\mathrm{Fe} = 0.29$.

The mass flux of oxygen to the particle surface is defined as

$$\dot{m}_{\mathrm{O}_2} = \frac{A_\mathrm{d}}{2r_\mathrm{p}}\mathrm{Sh}\rho_\mathrm{O2,f}D_\mathrm{f}X_\mathrm{O2,g}, \tag{4}$$

with $\rho_\mathrm{O2,f}$ and D_f respectively the oxygen density and diffusion coefficient at the film temperature and composition, Sh the Sherwood number, $X_\mathrm{O2,g}$ the mole fraction of oxygen in the surrounding gas, and A_d the diffusive surface area. The latter is the surface of the particle affected by the oxygen diffusion and is defined as $A_\mathrm{d} = 4\pi r_\mathrm{p}^2$.

The adapted model from Thijs et al. [14] solves a set of differential equations, describing the mass and energy balance between a reacting particle and the surrounding gas, to obtain the enthalpy evolution. The latter is then converted into a temperature evolution. The enthalpy varies due to the convective heat flux to the surrounding gas, the enthalpy gain due to the oxygen intake, the radiative heat flux to the surroundings, and the evaporative heat flux. This mathematically reads

$$\frac{\mathrm{d}H_\mathrm{p}}{\mathrm{d}t} = 2\pi\mathrm{Nu}r_\mathrm{p}k_\mathrm{f}(T_\mathrm{p} - T_\mathrm{g}) + \frac{\mathrm{d}m_\mathrm{p}}{\mathrm{d}t}h_{\mathrm{O}_2} + \epsilon\sigma(T_\mathrm{p}^4 - T_\mathrm{g}^4) + \sum_i \frac{\mathrm{d}m_{\mathrm{evap},i}}{\mathrm{d}t}h_{\mathrm{vap},i}, \tag{5}$$

with Nu the Nusselt number, k_f the gas thermal conductivity taken at the film conditions, T_p and T_g respectively the particle and gas temperatures, h_{O_2} the enthalpy of the oxygen absorbed, ϵ the emissivity of the particle, σ the Stefan-Boltzmann constant and $h_{\mathrm{vap},i}$ the enthalpy of each evaporated species i.

The mass evaporation rate of the different species is computed using a diffusion-limited evaporation represented by a Fickian diffusion: evaporated species diffuse far away from the particle before being oxidized. Using this assumption, the evaporation rate reads

$$\frac{\mathrm{d}m_{\mathrm{evap},i}}{\mathrm{d}t} = \frac{M_i p}{R_\mathrm{u}T_\mathrm{f}}A_\mathrm{p}k_{\mathrm{d,evap},i}X_{\mathrm{vap},i}, \tag{6}$$

with M_i the molar mass of species i, p the pressure, R_u the universal gas constant, T_f the film temperature, A_p the particle surface area, $k_{\mathrm{d,evap},i}$ the evaporation mass transfer coefficient and $X_{\mathrm{vap},i}$ the vapor molar fraction of species i.

The evaporated mass transfer coefficient is defined as

$$k_{\mathrm{d,evap},i} = \frac{\mathrm{Sh}D_{\mathrm{f},i}}{d_\mathrm{p}}, \tag{7}$$

with $D_{\mathrm{f},i}$ the diffusion coefficient of gaseous species i in air taken at the film conditions and d_p the particle diameter. Due to the lack of data concerning the diffusion coefficient of the gaseous impurities, it is assumed to be equal to that of FeO.

The vapor molar fraction of each species is computed using its intrinsic vapor pressure:

$$X_{\mathrm{vap},i} = X_{\mathrm{p},i}\frac{p_{\mathrm{v},i}}{p}, \tag{8}$$

with $X_{\mathrm{p},i}$ the molar fraction of species i inside the particle and $p_{\mathrm{v},i}$ the intrinsic vapor pressure of species i.

In reality, oxidation of gaseous iron could already start in the boundary layer. To model this, a boundary layer resolved model like the one by Thijs et al. [11] should be used but this is beyond the scope of this study. Also, treating the evaporation of each species independently using their intrinsic vapor pressure is a simplifying assumption. This amounts to considering that the evaporated mass of each species is defined by the intrinsic equilibrium between its liquid and gas phases. However, in reality, there exists a layer of air on top of these two layers in equilibrium which could change their equilibrium. The influence of this third layer is neglected as it would require a more detailed model specific to each impurity taking into account the mixed vapor pressures of all the elements together.

2.2.1. NO emissions

The production of NO emissions is implemented based on the thermal Zeldovich mechanism as detailed in supplementary material SM2. The O radical concentration is computed using the equilibrium approach: decoupling the thermal NO formation process from the main combustion mechanism. The NO formation rate is thus computed assuming an equilibrium of the combustion reactions. This gives

$$X_O = 3.97 \cdot 10^5\, T^{-1/2} X_{O2}^{1/2} e^{-31090/T}. \tag{9}$$

Even if during the combustion of a single iron particle its temperature exceeds 2000 K, the fraction of gas heated is limited to the boundary layer and the temperature may decrease considerably from the particle surface to the surrounding gas. Besides, the amount of oxygen available for NO formation decreases from the surrounding gas to the particle surface due to the oxidation of the particle. Therefore, NO production inside the particle boundary layer is negligible, as confirmed by Ravi et al. [33]. In this model, we assume that the NO formation zone is a film beyond the boundary layer where the oxygen concentration is 21 vol.% to keep a conservative estimation of NO emissions and the considered temperature for NO formation is computed using a coefficient α_{NO}:

$$T_{NO} = T_p + \alpha_{NO}(T_{gas} - T_p). \tag{10}$$

The coefficient α_{NO} lies between 0 and 1 representing a gas temperature equal to respectively the particle temperature and the surrounding gas temperature far from the particle. The calibration of the coefficient is performed for a pure iron case to qualitatively compare the impact of impurities on NO emissions in relation to the pure Fe case. The flame temperature during adiabatic oxidation with a stoichiometric mixture of air and pure iron is 2278 K [4] and is taken as an upper bound for the calibration. However, in reality, the gas temperature inside an iron flame is lower due to losses to the burner walls and the heterogeneity of the heat released. Baigmohammadi et al. [34] measured a gas temperature of 1150 K to 1250 K in their tornado burner. This value underestimates the gas temperature of a commercial burner because low equivalence ratios are used and the thermo-couples are not located in the hottest region of the flame. Still, it can be used as a lower bound. Regarding the two bounds for the gas temperature, several values of α_{NO} have been tested by the authors between 0.12 and 0.3 to keep a peak temperature for NO production between 1800 K and 2200 K.

2.3. Impure particle properties

Eqs. (1)–(8) require the evolution of the particle properties, which are impacted by the addition of impurities. For every material, the properties are found using TCOX11 and SSUB3 databases from the Thermo-Calc software respectively for liquid/solid phases and gaseous species. They are further detailed in supplementary material SM3.

In this work, a constant iron mass, and associated energy stored, are considered in the particles. The addition of impurities therefore increases the initial particle mass and diameter. The increase in diameter for a 50 μm-diameter pure iron particle to which 20 wt.% of impurity has been added ranges from + 5.19 μm for 20 wt.% of MnO to + 6.46 μm for 20 wt.% of SiO_2, which have respectively the highest and lowest mass densities of 5067 kg/m^3 and 2654 kg/m^3 at ambient conditions.

We consider two main particle properties impacted by the addition of impurities: (i) the absolute heat capacity and (ii) the mass density. It is assumed that the impurity content is homogeneously distributed inside the particle, except for sub-scenarios investigating the influence of the phase configuration described in Section 2.4.2. The influence of impurities on the particle's thermal conductivity and emissivity is neglected as demonstrated in supplementary material SM4.

The presence of impurities also modifies the combustion process due to: (iii) impurity melting, (iv) the creation of a complex ternary oxide, and (v) an inhomogeneous spatial distribution of the liquid-phases. Concerning point (iv), it will be analyzed using phase diagrams as they provide the complex phases that could be created from the reaction between iron, iron oxides, and metal oxide impurities. Nevertheless, the state described in phase diagrams is the chemical equilibrium state, which is not always reached due to the speed of the combustion process (a few ms). This depends on the diffusion speed of the different elements relative to the oxidation rate. In this work, two extreme cases are considered: either the oxidation reaction is much faster than the creation of a complex oxide, leading to separate phases, or the complex oxide reaction is much faster than the oxidation kinetics, leading to an instantaneous complex oxide formation when the impurity reaches the liquid state.

2.4. Parametric approach

2.4.1. Scenarios for the effects of specific heat capacity, mass density, melting and liquid-state interactions

To highlight the effect of each modified parameter and induced phenomena, three scenarios are defined and shown in Fig. 1. The initial state is always the same: A solid particle constituted of Fe and MOx. The iron particle temperature then rises due to oxidation. Melting is the first phase change occurring respectively at 1650 K for wüstite and 1811 K for iron.

Scenario 1 is intended to highlight the impact of the impurity's specific heat capacity and mass density. Impurity melting is not included, even when exceeding its melting temperature. The impurity properties above the melting point are computed as an extrapolation of the solid-state properties.

In scenario 2, the impact of including melting of the impurity is studied. The difference from scenario 1 is that part of the created heat is consumed by the melting process and the liquid-state properties of the impurity are used to compute the temperature and size evolution of the particle. However, even if the whole particle is in the liquid state, liquid elements are assumed to stay immiscible.

In scenario 3, liquid-state interactions are included. When two liquid oxide phases are mixed together, the chemical equilibrium might imply the creation of a complex ternary liquid oxide containing Fe, M and O at a variable composition. The latter is generically denoted as FeM_yO_z in the following. For each MO_x concentration, a specific analysis of the Fe-FeO-MO_x system must be conducted. In this work, we only consider that the reaction between liquid FeO and liquid MO_x could create a complex phase. In reality, liquid Fe could also be involved and lead to a phase separation into a distinct Fe-rich and M-rich oxide phases. For simplicity and as liquid FeO is more present than liquid Fe when the impurity melts, the complex phase composition is extrapolated from the reaction in solid state between FeO and MO_x. For example with Al_2O_3, the liquid-state reaction is

$$FeO_{(l)} + Al_2O_{3(l)} \longrightarrow FeAl_2O_{4(l)}. \tag{11}$$

We assume in this third scenario that the reaction above is much faster than oxidation kinetics, leading to an instantaneous complex oxide formation when the impurity melts. Based on a cross-analysis between literature [38–40] and the TCOX11 database from the Thermo-Calc software, the binary phase diagram of each impurity with FeO indicates a production of $FeAl_2O_4$, Fe_2SiO_4 and $(Fe,Mn)_{(1-x)}O$. CaO is not considered due to its high melting temperature of 3200 K. Mathematically, after the instantaneous conversion of all the impurity and the associated mass of FeO, Eq. (3) is replaced by

$$\frac{dm_{FeMyOz}}{dt} = -\frac{dm_{evap,FeMyOz}}{dt}, \tag{12}$$

and the properties of the complex oxide phase are included.

2.4.2. Scenarios about liquid-state configurations

The spatial distribution of the liquid phases during the combustion process depends on the wettability between the phases and the interface energies [41]. A dedicated study of the wettability between the phases

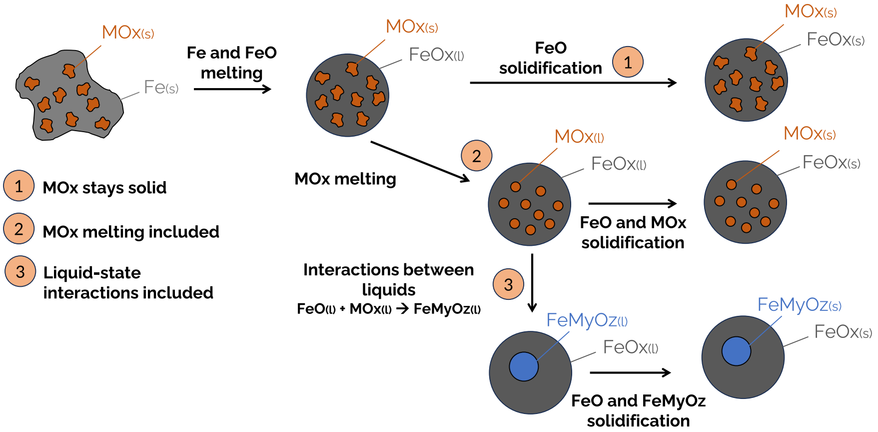

Fig. 1. The parametric procedure leads to three different scenarios: (1) No impurity phase change, (2) impurity melting and solidification without liquid-state interactions, (3) liquid-state interactions included.

for each system Fe-FeO-MO_x could be conducted but is beyond the scope of this work. However, in addition to the general case of a homogeneous distribution of the phases within the particle, we consider four auxiliary sub-scenarios starting when the impurity melts. Once the whole particle is in the liquid state, the melted impurity might move either to the core or to the surface of the particle. As presented in the previous Section 2.4.1, the melted impurity can also react with liquid iron oxide. This gives the four sub-scenarios illustrated in Fig. 2. Sub-scenarios 2bis and 2ter are respectively associated with an impurity shell and an impurity core. Physically, they represent a case where the impurity moves either to the surface (2bis) or to the center (2ter) of the particle, without reacting with liquid iron oxide. Sub-scenarios 3bis and 3ter are similar to sub-scenarios 2bis and 2ter but liquid-state interactions are included leading to the creation of a complex oxide. In all sub-scenarios, we assume that the liquid phases take the new spatial configuration instantaneously after reaching impurity melting, assuming an infinitely faster movement of the liquid phases compared to the oxidation rate. Also, the liquid mixture of Fe and FeO is considered homogeneous, both in the core and the shell.

The new spatial distributions taken by the liquid phases impact the oxidation rate by modifying the particle radius used to compute the diffusive surface area (see Eq. (4)). As only Fe consumes oxygen, the internal radius is used in sub-scenarios 2bis and 3bis because iron is concentrated in the core. This gives:

$$A_d = 4\pi r_{int}^2, \tag{13}$$

with r_{int} being the internal radius computed as $r_{int} = r_p - \delta$, where δ is the thickness of the impurity or complex oxide shell (as illustrated in Fig. 2 for sub-scenario 2bis). Physically, this means that the shell behaves as a porous inert layer, maintaining the assumption of an infinitely fast internal diffusion of oxygen. This assumption is discussed later in Section 3.5. For sub-scenarios 2ter and 3ter, as liquid Fe is located at the surface of the particle, the total radius of the particle is used as in Eq. (4).

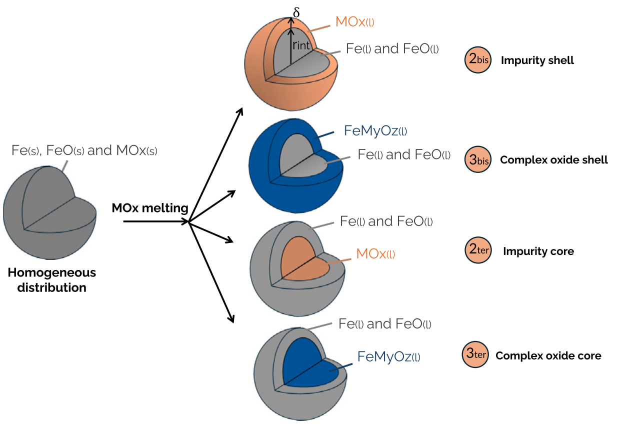

Fig. 2. Four auxiliary sub-scenarios are tested with a different spatial distribution of the liquid phases after the impurity melts: The impurity shell (2bis), the complex oxide shell (3bis), the impurity core (2ter) and the complex oxide core (3ter).

The spatial distributions of the liquid phases impact evaporation. As the latter is a surface process, only the species located in the shell will evaporate. In sub-scenarios 2bis and 3bis, the only species to evaporate are respectively MO_x and FeM_yO_z, preventing Fe and FeO from evaporating. Similarly, only evaporation of Fe and FeO is considered in sub-scenarios 2ter and 3ter. For each species, the evaporation is computed using Eqs. (6)–(8).

2.4.3. *Output parameters*

The influence of impurities is analyzed using three combustion parameters: (i) the peak temperature, (ii) the time to peak temperature, and (iii) the liquid combustion time (LCT). The latter is the time between the start of iron melting and the peak temperature (as defined by Ning et al. [42]).

The mass evaporated depends on the composition of the liquid in contact with the surrounding gas and on the temperature as it dictates the equilibrium vapor pressure. Therefore, the peak temperature is related to nanoparticle formation: The higher the temperature, the higher the vapor pressure and the more nanoparticles are created. Another parameter influencing nanoparticle formation is the LCT, which is directly correlated to the evaporation time (Eq. (6)). Also, Huang et al. [5] suggested that micro-explosions result from the creation of a gas inside the particle and that the temperature gradient between the particle and the surrounding gas plays an important role in the micro-explosion behavior. Although a dedicated experimental study of the influence of the particle temperature on the probability of micro-explosion should be conducted, a lower particle temperature would lead to a lower probability of internal boiling and a smaller temperature gradient which might reduce the occurrence of micro-explosions. Therefore, a positive impact of the presence of impurities inside the particle would be a decrease in the peak temperature with the same amount of heat released. Although NO emissions are already at a low level for iron combustion, the decrease in peak temperature and LCT also reduces them.

Another important parameter is the powder energy density. Keeping the same amount of pure iron in the initial powder means the same

Table 1
Initial conditions corresponding to the combustion of an ignited impure particle with a varying impurity content in an ambient environment.

Inputs	Symbol	Value
Initial particle temperature [K]	$T_{\mathrm{p,in}}$	1100
Gas temperature [K]	T_{gas}	300
Oxygen concentration [vol.%]	$X_{\mathrm{O_2}}$	21
Initial iron mass [kg]	$m_{\mathrm{Fe,0}}$	$5.15 \cdot 10^{-10}$
Impurity concentration [wt.%]	Y_{MOx}	0 - 20

amount of energy is contained. However, the added impurity decreases the energy density. Compared to a pure iron powder, a larger volume and mass of impure powder are needed to transport and store the same amount of energy. A quantification of this decrease in energy density and the impact on the power of a practical burner is presented and discussed in Section 3.4.

2.5. Initial conditions

The model simulates the combustion of an ignited particle initially at 1100 K inside ambient gas at 300 K and 21 vol.% oxygen concentration. In all cases, the mass of iron remains equal to $5.15 \cdot 10^{-10}$ kg, the mass of a pure iron particle with 50 μm diameter. The common set of initial conditions used is presented in Table 1.

3. Results and discussion

3.1. Overall temperature evolution

The presence of impurities impacts the temperature evolution. As an illustration, the impact of the modified heat capacity and mass density is represented in Fig. 3 using scenario 1. In that case, the presence of 20 wt.% of Al_2O_3 decreases the peak temperature by 124 K. The time to iron melting increases by 1.78 ms and the time to the peak temperature decreases by 1.48 ms. Together, they lead to a difference of 3.26 ms in LCT.

3.2. Characteristic combustion time scales

3.2.1. Impact of changing heat capacity and mass density

The time to peak temperature is driven by the oxidation rate. The higher the impurity concentration, the larger the particle diameter, especially for low-density impurities like SiO_2. However, a higher particle diameter means a larger diffusive surface area, increasing the oxidation rate (see Eq. (4)). As oxygen diffusion to the particle surface is assumed to be the only rate-limiting mechanism, an increase in the particle diameter leads to a decrease in the time to peak temperature. In scenario 1 with 20 wt.% of SiO_2, the lowest-density impurity, the time to peak temperature decreases by 11.5 %.

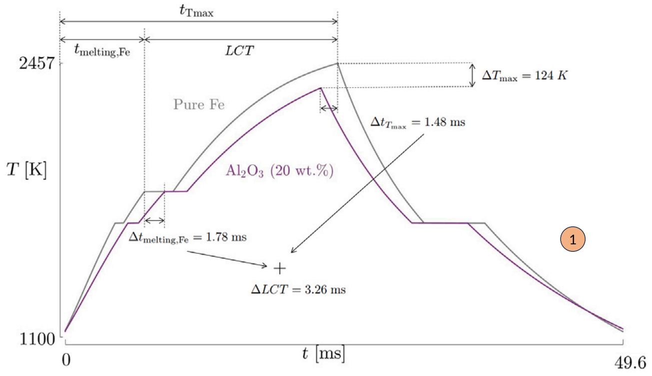

Fig. 3. The temperature evolution for pure iron is compared to a case with 20 wt.% of Al_2O_3 using scenario 1. The peak temperature decreases by 124 K. The time to iron melting increases by 1.78 ms and the time to the peak temperature decreases by 1.48 ms. Combining both impacts leads to a decrease in LCT of 3.26 ms.

With an increased absolute heat capacity, the particle requires more energy to reach iron melting temperature. The time to iron melting therefore increases with the impurity concentration, especially for impurities with a high specific heat capacity like Al_2O_3 featuring an increase of 25.6 % from 0 to 20 wt.%.

As the time to peak temperature decreases due to the lower mass density and the time to iron melting increases due to the higher absolute heat capacity, the LCT decreases with the impurity concentration as it is the difference between the two. The decrease is accentuated for impurities combining a high specific heat capacity and a low mass density. Therefore, SiO_2 features the highest decrease in LCT of 23.1 % (from 16.96 ms at 0 wt.% to 13.05 ms at 20 wt.%). For the other impurities at 20 wt.%, the decrease equals 19.2 %, 18.2 %, and 13.9 % ms respectively for Al_2O_3, CaO, and MnO.

3.2.2. Impact of the liquid phase's spatial distribution

The presence of a shell (2bis and 3bis) involves a longer LCT, while the latter does not change with the presence of a core (2ter and 3ter). The time to iron melting is not influenced by the liquid phase's spatial distribution as the sub-scenarios (Fig. 2) all start when the impurity melts. The change in the time to peak temperature is thus equal to that in LCT. As presented in Section 2.4.2, the presence of a shell reduces the diffusive surface area to the internal core of iron and iron oxide. This implies a lower oxygen flux, a lower oxidation rate and subsequently a higher LCT. As the presence of an impurity/complex oxide core (2ter and 3ter) does not impact the diffusive area, it does not influence the LCT. A thicker shell leads to a higher relative variation of the LCT as it reduces the volume of the internal sphere. Therefore, a shell of the lowest-density impurity (SiO_2) leads to the biggest relative increase in LCT of 17 % compared to a homogeneous case. This value is even bigger (+55.3 %) with the presence of a complex oxide shell (3bis) due to the fraction of FeO moved from the internal core to create the complex oxide in the shell. The increase in LCT reaches 5.8 % and 11.5 % respectively for a MnO and $(Fe,Mn)_{(1-x)}O$ shell due to the higher mass density of MnO and the lower fraction of FeO inside the complex oxide. Concerning an Al_2O_3 shell, it induces a low increase in LCT of 1.5 % due to the limited impurity concentration still leading to full melting as explained in Section 3.3.2.

3.3. Peak temperature, evaporation and NO emissions

3.3.1. Impact of changing heat capacity

Increasing the absolute heat capacity with the same heat release decreases the peak temperature. Oxide impurities act as a thermal buffer, absorbing part of the heat that previously increased the pure iron particle temperature. Therefore, a lower peak temperature is reached especially for impurities with a high specific heat capacity: Using scenario 1, 20 wt.% of impurity decreases the peak temperature by 124 K for Al_2O_3 and SiO_2, by 97 K for CaO, and by 82 K for MnO compared to a pure iron case.

3.3.2. Impact of impurity melting

Two properties drive the impact of impurity melting on the peak temperature: The melting temperature (T_{melting}) and the specific latent heat of melting (q_{melting}), both listed in Table 2. CaO is not affected as the peak temperature (2457 K at a maximum) never reaches its melting temperature (3200 K). For MnO and SiO_2, the melting temperature (respectively 2120 K and 1996 K) is always reached in the considered range of impurity concentration. Therefore, as shown in Fig. 4 using scenario 2, the peak temperature continuously decreases with the impurity concentration. This is due to both the effect of the heat capacity and that of melting. For Al_2O_3, the melting temperature (2345 K) is only reached with an impurity concentration lower than 8.3 wt.%. Therefore,

Table 2

Melting temperature and specific latent heat, also reported relative to the LHV of iron assuming oxidation to FeO, of the considered impurities. Due to its high T_{melting}, CaO does not melt. The two elements with the highest q_{melting} are Al_2O_3 and MnO.

Impurity	Al_2O_3	SiO_2	MnO	CaO
T_{melting} [K]	2345	1996	2120	3200
q_{melting} [kJ/kg$_{\text{MOx}}$]	1102	149	601	1420
$q_{\text{melting}}/LHV_{\text{Fe}\rightarrow\text{FeO}}$ [%]	22.6	3.1	12.3	29.2

a plateau of peak temperature corresponding to its melting temperature is obtained when considering a concentration up to 18.4 wt.% (see Fig. 4). The plateau starts when Al_2O_3 does not melt completely anymore, transitioning from full to partial impurity melting. In that case, the heat released by iron oxidation is high enough to reach the impurity melting temperature, but not enough to completely melt it. Only a fraction is melted so the peak temperature remains equal to the melting temperature. This fraction decreases along the plateau due to the increased absolute heat capacity. Partial melting ends when the impurity melting temperature is no longer reached. Afterward, only the effect of the increased absolute heat capacity decreases the peak temperature, explaining the lower slope compared to full melting. The presence of an impurity with a melting temperature close to but lower than the predicted peak temperature could therefore be used to control the flame temperature.

When impurity melting is included, the peak temperature significantly decreases: A decrease of 64 K and 70 K is observed respectively for MnO at 20 wt.% and Al_2O_3 at 8.3 wt.% (see Fig. 4). The lower decrease of 19 K for SiO_2 at 20 wt.% is explained by its lower q_{melting} of 149 kJ/kg compared to 601 kJ/kg and 1102 kJ/kg respectively for MnO and Al_2O_3. When including impurity melting, the peak temperature evolution for MnO and SiO_2 is similar due to the high q_{melting} of MnO despite a lower specific heat capacity than SiO_2. In summary, the decrease in peak temperature is the highest for an impurity with a high q_{melting} and the highest concentration possible while still guaranteeing full melting.

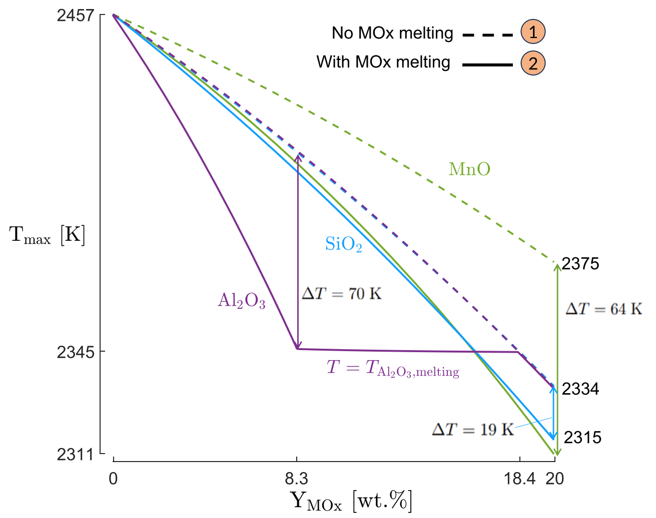

Fig. 4. Impurity melting decreases the peak temperature, especially with a high MO_x concentration and q_{melting} when full impurity melting occurs. Cases with solid curves include impurity melting while those with dashed curves do not. The full melting region might be limited up to a certain concentration depending on T_{melting} of the impurity like for Al_2O_3. In that case, partial melting occurs and the peak temperature evolution plateaus at T_{melting}.

3.3.3. Impact on NO emissions

NO production is governed by the evolution of O radicals' concentration, determined by the gas concentration and temperature (Eq. (9)). As oxide impurities do not consume oxygen during combustion, their main influence on NO emissions comes from their impact on temperature. Using scenario 2, Al_2O_3 is the most efficient in reducing NO emissions for an impurity addition of up to around 10 wt.% (depending on α_{NO}), with more than 50 % NO reduction for an addition of 5 wt.% (see Fig. 5). For a larger impurity concentration, SiO_2 and MnO are the most efficient: A reduction of 90 % is achieved for an addition of 20 wt.% of MnO or SiO_2.

As explained in Section 2.2.1, a tuning value α_{NO} varying between 0.12 and 0.3 is used to determine the gas temperature relevant for NO production, between 1800 K and 2200 K. Regarding the small thickness of shaded areas in Fig. 5, the relative evolution of NO emissions is not strongly impacted by α_{NO}. Only the absolute values change: Between 30.7 and 3.6 mg/m^3 for $\alpha_{\text{NO}} = 0.12$ and between 0.045 and 0.004 mg/m^3 for $\alpha_{\text{NO}} = 0.3$ from a pure iron case to 20 wt.% of MnO. As a comparison, Wiinikka et al. [25] measured NO emissions between 31.5 and 36.2 mg/m^3 in an iron flame and Baigmohammadi et al. [34] measured a NO production between 14.8 and 21 mg/m^3. These values are more similar to those obtained with $\alpha_{\text{NO}} = 0.12$. However, the presence of water vapor during the experiments could have enhanced NO production by increasing the concentration of OH radicals as numerically observed by Ravi et al. [33]. Therefore, a high uncertainty still remains regarding the exact value of α_{NO} which justifies the range taken in this work.

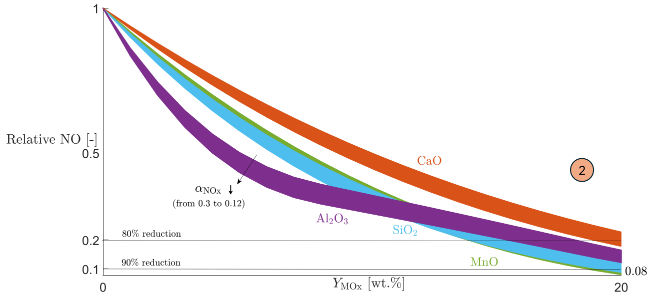

Fig. 5. NO emissions decrease with MO_x concentration due to the associated lower temperature level. They are represented relatively to a pure iron case. The shaded area represents the relative NO emission for a coefficient α_{NO} varying between 0.12 and 0.3. Below a concentration of 10 wt.%, Al_2O_3 features the biggest decrease, while it is MnO and SiO_2 at higher concentrations.

3.3.4. Impact on evaporation

Two main parameters influence evaporation: The temperature and the LCT. The vapor pressure of each element increases with temperature, dictating the evaporation rate, while the LCT defines the evaporation duration period. The indicator used to quantify the total amount of evaporation is the total relative mass evaporated, namely the sum of all gaseous species divided by the mass of the particle. As illustrated in Fig. 6, it decreases with the impurity concentration: Below a concentration of around 10 wt.%, Al_2O_3 features the biggest decrease with 0.111 wt.% evaporated at 5 wt.% compared to 0.182 wt.% for pure iron. Above 10 wt.%, SiO_2 becomes the impurity involving the lowest total evaporation with 0.029 wt.% at 20 wt.%. The values obtained for the total relative evaporation are comparable to the measurements of Prasidha et al. [26] between 0.01 wt.% and 0.13 wt.% of iron evaporated, but well below the other measurements between 1.2 wt.% and 20 wt.% [6,25,27–29]. Despite the non-negligible experimental uncertainties associated with the varying experimental conditions (flame configuration, oxygen concentration, iron particles, gas composition), the low estimation of the current model for the mass evaporated comes from the assumption of a diffusion-limited evaporation (see

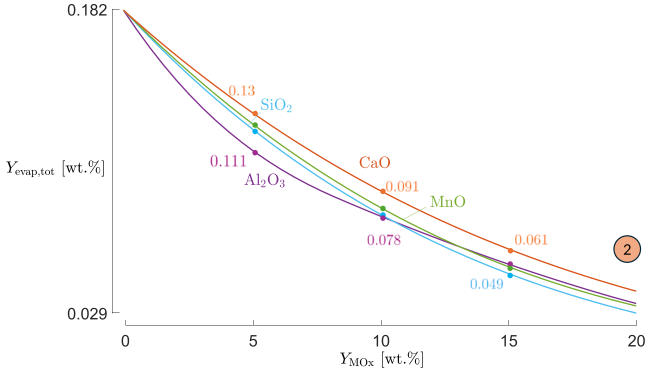

Fig. 6. The evaporated mass of all species reported on the total mass of the particle decreases with MO_x concentration due to the decrease in peak temperature. Below 10 wt.%, Al_2O_3 features the biggest decrease in evaporation while above that point it is SiO_2.

Section 2.2). As discussed by Chang et al. [29], this assumption corresponds to the slowest mechanism of evaporation, representing a lower bound. Another approach consists of assuming a surface-kinetic-limited evaporation regime for which the evaporation rate is limited by the rate at which evaporated molecules move away from the liquid surface. As shown in their numerical simulations, this gives an estimation of the upper bound of the iron mass evaporated (close to 5 wt.% for 21 % oxygen). In addition, the work of Nguyen et al. [21] showed that resolving the boundary layer by including gaseous reactions, i.e., starting from liquid FeO as the first precursor, may lead to larger estimations of the mass evaporated (between 6 and 12 wt.%). As the exact mechanism for nanoparticle formation is still unclear, and even more so when impurities are present, further work is still needed both to extend experimental datasets in different experimental conditions and to improve existing numerical models.

Among the different species, Fe and FeO evaporate most. The most evaporative impurity is MnO. However, even at 20 wt.% of MnO, its evaporation accounts for only 16 % of the total mass evaporated (0.03 wt.%) while that of Fe and FeO accounts for 46.5 % and 37.5 %. As evaporation is a surface process, it is highly influenced by the spatial distribution of the liquid phases: Only the species present at the particle surface evaporate. Using the sub-scenarios described in Fig. 2, the largest decrease in total mass evaporated occurs when an impurity shell forms (2bis) (from -46 % for Al_2O_3 to -82.8 % for SiO_2 compared to a homogeneous case). This results from the limited evaporation of Fe and FeO inside the core. The mass evaporated therefore depends on the propensity of the impurities or complex oxides to evaporate. Subsequently, the presence of a complex oxide shell (3bis) leads to more evaporation than an impurity shell (2bis): The total mass fraction evaporated decreases by 17.1 % with a Fe_2SiO_4 shell compared to 82.8 % with a SiO_2 shell. When an impurity core (2ter) forms, it only prevents liquid MO_x evaporation and leads to a smaller decrease in total mass fraction evaporated as iron (oxide) evaporation represents most of the mass evaporated. These results show that estimating evaporation requires a good understanding of the liquid-phase configuration and especially of the surface composition.

According to the current results, the presence of impurities mitigates evaporation and mass losses. Nevertheless, the uncertainty about the exact phase distribution during impure iron particle combustion complicates the liquid-gas interaction at the basis of the evaporation process. Large variations from the predictions of the homogeneous case could be obtained in case of inhomogeneous spatial distribution of the liquid phases within the particle.

3.3.5. Impact of liquid-state interactions

Liquid Al_2O_3, SiO_2 and MnO can react endothermically with FeO to form a complex oxide phase. Table 3 presents the enthalpies corresponding to the formation of this phase. Using scenario 3, a decrease in peak temperature of 10.4 K, 35.4 K, and 31.5 K is achieved respectively with 7.8 wt.% of Al_2O_3, 20 wt.% of SiO_2, and 20 wt.% of MnO. Two comments should be made here. First, the Al_2O_3 concentration leading to the biggest decrease in peak temperature is now 7.8 wt.% compared to 8.3 wt.% previously. This results from a shift of the limit between full and partial melting due to the heat necessary to create the complex oxide phase. Second, the decrease in peak temperature is slightly greater with SiO_2 than MnO despite the lower formation energy of $FeAl_2O_4$. This is due to the 1.7 times more mass of complex oxide created with 20 wt.% of SiO_2 than with 20 wt.% of MnO.

Table 3
Melting temperature and formation energy of each complex ternary oxide created when reacting with FeO. The formation reaction is slightly endothermic. Current data were obtained using the TCOX11 database from the Thermo-Calc software.

Complex oxide	$FeAl_2O_4$	Fe_2SiO_4	$(Fe,Mn)_{(1-x)}O$
Melting temperature [K]	2289	1475	1868
Formation energy [kJ/kg_{FeMyOz}]	18	94	113
Formation energy/$LHV_{Fe \rightarrow FeO}$ [%]	0.4	1.9	2.3

The presence of a complex oxide phase also modifies evaporation. As presented in supplementary material SM3, its intrinsic vapor pressure is close to that of the oxide impurity at its origin. Therefore, the fraction of FeO used to create the complex oxide evaporates according to that vapor pressure rather than that of FeO. The impact on evaporation is therefore greater when a high proportion of FeO is needed to create the complex oxide and when its vapor pressure is very different from that of FeO. Therefore, the largest difference occurs for SiO_2 as Fe_2SiO_4 requires most mass of FeO per mass of impurity: At 20 wt.%, the relative total mass fraction evaporated goes from 0.029 wt.% to 0.035 wt.% when including liquid-state interactions. In that case, the mass evaporated increases due to the higher tendency of Fe_2SiO_4 to evaporate compared to FeO. For MnO and Al_2O_3, the impact is negligible due to the lower mass of FeO required or the smaller difference in vapor pressure.

3.4. Energy density and power of a practical burner

The presence of an inert element decreases the powder energy density, especially with low-density impurities: A powder containing 20 wt.% of SiO_2 exhibits a decrease in energy density of 37.2 % compared to 23.7 %, 28.3 % or 32 % with 20 wt.% of MnO, Al_2O_3 or CaO. The consequence of the lower energy density is increased transport and storage costs. A dedicated economic analysis should be conducted to quantify these costs and find the trade-off between the savings from the production and the extra transport and storage costs.

The decrease in energy density leads to a decrease in power for a burner using impure powder. To quantify this, let us consider a 12 MW biomass-fired boiler as described in [43] converted into an impure iron powder burner. For a pure iron case, it burns 1.7 kg/s of powder with a degree of oxidation of 50 % magnetite and 50 % hematite as achieved in [23,34]. For the different impurities, we assume the same oxidation degree and a constant powder volume flow rate. In practice, the amount of injected powder is limited by the range of volume flow rates allowed by the injection system, either to ensure a self-sustained flame for the minimum flow rate, or as imposed by the design limits and flame stability for the maximum flow rate. Therefore, when increasing the impurity concentration, part of iron is replaced by an impurity which decreases the power (see Fig. 7). Similar to the energy density, power decreases more for low-density impurities. At 5 wt.% impurity concentration, the power decreases from 12 MW to between 10.5 MW and 11.2 MW respectively for SiO_2 and MnO. At 20 wt.%, it decreases to between 7.5 MW and 9.2 MW.

As presented in Section 3.2.1, the presence of impurities decreases the combustion time. This might decrease the size of the flame and the

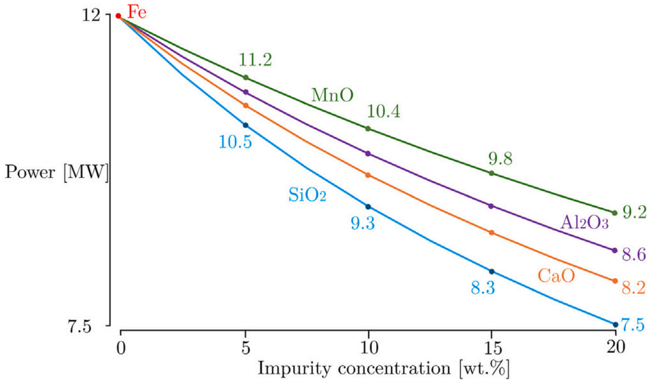

Fig. 7. Power evolution of a practical impure iron powder burner inspired by a 12 MW biomass-fired boiler [43]. The power decreases with the impurity concentration, especially with low-density impurities.

injected powder flow rate might need to be adapted. One could consider oversizing the powder feeding system to maintain a constant power regardless of the impurity concentration. However, the large variability of the impurity concentration in low-cost unvalued iron sources makes it difficult to control this parameter. On the contrary, the design of a burner dedicated to impure iron powder should be able to handle a large variability in its power. A future study should be dedicated to the control of the flame when varying composition of impurity-containing iron powders.

The energy density can also be decreased by the formation of complex oxides, preventing full oxidation of Fe. A more detailed study about the kinetics underlying the competition between complex oxide formation and oxidation of FeO should be conducted. Yet, the upper limit of the fraction of energy not released can be estimated based on a worst-case scenario by assuming that all the FeO used to create the complex oxide cannot be further oxidized. The decrease in energy release is particularly important for Fe_2SiO_4 with 20.3 % of energy not released due to the higher proportion of FeO needed (70.5 % in Fe_2SiO_4 compared to 40.7 % and 50.3 % in $FeAl_2O_4$ and $(Fe,Mn)_{(1-x)}O$, respectively).

The results and discussion presented in this section suggest that a stable flame is achieved regardless of the impurity content. However, impurities may affect the ignition temperature of the powder, which in this study is assumed to be constant and equal to that of pure iron. A reduction in ignition efficiency could negatively impact flame stability. Therefore, additional experimental ignition tests on impure powders should be performed, complemented by advanced CFD simulations.

3.5. *Impact of model assumptions*

In this study, the combustion regime is limited only by the external diffusion of oxygen to the particle surface, assuming that oxygen surface chemisorption and internal ion diffusion occur infinitely fast. While it has been presented in Section 1 that including these mechanisms provides a better fit for the temperature evolution during the initial heating rate and the peak temperature, it is still not possible to extend the work done on pure Fe to impure cases. First, to include surface chemisorption as in [15], dedicated reactive force fields of Fe-O-MOx systems must first be identified, as the results are highly sensitive to them [44]. Second, the uncertainty regarding the high-temperature oxygen diffusion coefficient inside iron and its oxides becomes more pronounced when considering layers of MO_x or complex oxides. This hinders a proper prediction of the limiting mechanism in impure particle combustion.

To overcome the lack of internal diffusion coefficient, the oxygen internal diffusion rate used by Fujinawa et al. [16] in their heuristic model was used for iron oxide and divided by a factor from 1 to 10 for the oxide impurities. This value has been chosen based on a measurement of the oxygen diffusion coefficient inside Al_2O_3 [45] showing that it is expected to be lower than that inside FeO by at least one order of magnitude. Decreasing the oxygen diffusion coefficient by a factor of 10 makes the combustion internal-diffusion limiting from the beginning. Therefore, the presence of impurities with a low oxygen diffusion coefficient is expected to lead to a combustion regime more limited by the internal diffusion, as also suggested by Peng et al. [8] due to a Si-containing oxide layer. From their results, it can be expected that the combustion time of the particles increases due to a mitigated oxidation rate of the core, or that the particles feature several local temperature peaks resulting from a consecutively increased and decreased oxidation rate. Nevertheless, too many unknowns remain to accurately model the combustion of an impure iron particle including all rate-limiting mechanisms. Oxygen internal diffusion coefficient inside iron oxide and the oxide impurities should be measured experimentally. Besides, although recent studies [46–48] suggest that a core-shell structure between liquid iron and liquid iron oxide takes place, the configuration of the phases when an impurity is present is yet unclear. It will modify liquid-phase properties such as the wettability, the surface energy, etc. All of this makes the internal-diffusion-limited regime too difficult to be accurately modeled at this point. Therefore, further research is required to investigate the impact of internal transport.

3.6. *Recyclability*

According to the Ellingham diagram, iron oxides have a higher tendency to be reduced using hydrogen than the other considered metal oxides [49]. Therefore, the resulting particle from an ideal reduction process where all iron is reduced is composed of pure iron and the oxide impurities. Reducing the oxide impurities would require more energy or another species for the reductant gas. Therefore, non-volatile impurities remain in the oxide form throughout the consecutive combustion-reduction cycles.

It is important but difficult to predict the influence of oxide impurities on the reduction of impure iron powder because it depends on several operating conditions. Their impact could vary depending on the reduction temperature, the impurity concentration or its distribution within the particle. The current gap in knowledge mainly arises from the lack of experimental data. Yet, a few studies discussed in the work of Choisez et al. [4] have addressed the influence of oxide impurities during hydrogen-based direct iron reduction and the literature review will be further extended in this section.

The influence of impurity addition on the reduction of iron oxides, such as SiO_2, CaO, Al_2O_3 and MnO, has been mostly studied in the context of reducing iron ore pellets in blast furnaces. The change in porosity and surface area of the initial pellets with the addition of impurities can have a major impact on the reduction kinetics. Yet, the combustion products expected in the context of iron fuel present different morphology and porosity as compared to the pellets. Therefore, the impact of doping on the reduction kinetics via their influence on the initial morphology of the pellets should be disregarded in this context. Several observations made in these studies can nevertheless provide insights into the positive/negative influence that can be expected from these doping elements on the reduction process.

Si enters into solid-solution in hematite with up to 5 wt.% SiO_2 addition [50,51], after which an additional presence of SiO_2 phase was detected [52]. During the reduction process, the reaction between FeO and SiO_2 leads to the formation of Fe_2SiO_4 [50,52–54] and other silicates such as $Fe_{0.67}Si_{0.08}O$ [53,55]. These silicates exhibit a lower reducibility and their formation decreases the porosity of the pellet [53–55]. Consequently, a shift towards lower diffusion-limited reduction kinetics is observed at the end of the reduction process in the range of 800 °C to 1100 °C [50,53–56]. A significant decrease in the reduction kinetics was also reported for temperatures over 1200 °C, due to the formation of a dense Fe layer at the boundary between the gas phase and a Si-rich liquid oxide at the surface of the particle [57]. A strong inhibition effect of Si-doping on hematite-dense thin film during its reduction process at 700 °C under Ar and 5 % H_2 was also reported due to the formation of a Si-rich oxide layer at the film surface [58].

Ca enters into solid-solution in FeO up to its solubility limit (around 5.8 wt.%) [54], after which the complex oxide $Ca_2Fe_2O_5$ is stabilized, after pelletization at 1000 °C [54]. The addition of CaO to FeO is associated with an expansion of the FeO lattice parameter, promoting Fe reduction through a faster cationic diffusion [53,54]. Moreover, CaO addition has been linked to a more porous morphology of the reduced Fe, promoting gaseous diffusion [59]. Wang et al. [51] also claimed that CaO-doping of FeO increases the nucleation site density for reduced Fe. A global increase in the reduction kinetics was reported with the addition of CaO in presence of Si-doped hematite pellets [51]. A higher reducibility is reported for basic briquettes compared to acidic briquettes, i.e., for a high ratio of CaO/SiO_2, especially at high reduction temperatures (900 °C). When both CaO and Al_2O_3 are added to dense FeO, the reduction rate using H_2 in the range 670–930 °C increases with CaO content due to the promotion of a more porous reduced Fe layer [60].

Depending on the pelletization temperature and amount of Al_2O_3, Al can enter into solid-solution in Fe_3O_4 or stabilize $FeAl_2O_4$ phase [61]. During the reduction of Fe_3O_4 to FeO, Al cations migrate from the reduced FeO to the unreduced Fe_3O_4 due to their low solubility in FeO [62,63]. Al enrichment in Fe_3O_4 leads to the stabilization of $FeAl_2O_4$ at the interface between FeO and Fe_3O_4 [62]. The strong volume changes between reduced FeO and $FeAl_2O_4$ lead to local crack formation at their interface, which is accelerated in the case of large initial Fe_3O_4 grains [62]. The dynamic cracking is associated with an increase in surface area, accelerating the reduction kinetics of the pellets with the addition of 1 to 4 wt.% of Al_2O_3 in Fe_3O_4 pellets using CO as a reducing agent at 950 °C [62]. A similar acceleration of the reduction kinetics was reported for the addition of 3 wt.% of Al_2O_3 in Fe_3O_4 pellets, reduced using CO gas at 750–850 °C [63]. However, increasing the amount of Al_2O_3 addition to 6 wt.% strongly reduced the reduction kinetics, and nearly stopped the reduction process for 12 wt.% of Al_2O_3 [63]. This negative effect was associated with the lower reduction temperature compared to the work of Paananen et al. [62]. Below 850 °C, thermodynamics require a direct phase transformation from Fe_3O_4 to $FeAl_2O_4$ with further Al enrichment, which is kinetically complicated due to the complex cationic rearrangement required [63]. Consequently, the reduction of Fe_3O_4 to FeO stops once the solubility limit of Al in magnetite is reached [63]. A general decrease in hydrogen-based reduction kinetics at low temperatures (300–500 °C) was also reported with the addition of 0.5 to 5 wt.% of Al_2O_3 in Fe_2O_3 pellets [64]. Above 850 °C, a solid solution of Al in Fe_3O_4 is thermodynamically possible up to the formation of $FeAl_2O_4$, allowing a larger reduction level to be reached, and improving the reduction kinetics by the formation of cracks [61–63]. The addition of 0.5 wt.% of Al_2O_3 in dense FeO plates resulted in low reduction kinetics due to the formation of a dense outer Fe layer, preventing the diffusion of the reactant hydrogen gas to the reaction interface [60]. Yet, increasing Al_2O_3 addition to 1 to 5 wt.% of Al_2O_3 accelerated the reduction kinetics due to the local distortion of the lattice around $FeAl_2O_4$ precipitates [60].

The addition of 2 to 6 wt.% of MnO_2 in Fe_2O_3 pellets resulted in the formation of $MnFe_2O_4$ phase, due to the reduction of MnO_2 into MnO, which reacts with Fe_2O_3 to form $MnFe_2O_4$ [50]. The formation of these complex ternary oxides reduces the reduction kinetics under 1000 °C [65] due to the low reducibility of $MnFe_2O_4$ [66] and the formation of dense Mn-doped FeO phase [65]. An acceleration of the reduction kinetics was observed over 1000 °C due to an increased swelling phenomenon with the formation of these ternary oxides, increasing the surface area of the pellets due to the formation of micro-cracks on the surface [50]. The addition of both MnO_2 and SiO_2 in Fe_2O_3 pellets results in strong decrease in the reduction kinetics due to the formation of low reducible $(Fe,Mn)_2SiO_4$ phase [50].

To summarize, a general negative effect of Si and Mn oxide impurities can be expected on the reduction kinetics of combusted Fe oxide, due to the low reducibility of the complex ternary oxide phases formed. The addition of Al_2O_3 can favor the reduction kinetics through a local distortion of the crystal lattice and/or dynamic cracking under the condition of stabilizing the hercynite phase. A general positive effect can be expected with the addition of CaO due to the expansion of the crystal lattice of wüstite, an increased density of nucleation sites for Fe and a more porous morphology of the reduced Fe. This literature review shows that it may change with each specific impurity, in each specific experimental condition (morphology of the products to be reduced, concentration, temperature, etc). Subsequently, more experimental studies of the reduction of impure powders with varying impurity compositions and under varying experimental conditions are recommended.

4. Conclusion and work perspectives

Using a fully external-diffusion-limited single-particle combustion model, the goal of this study was to improve our understanding of the impact of four non-volatile oxide impurities present in iron powders with a varying concentrations from 0 wt.% to 20 wt.%: Al_2O_3, SiO_2, MnO, and CaO.

The presence of these impurities decreases the peak temperature (up to 146 K with 20 wt.% of MnO) due to the additional mass inside the particle and the impurity melting. Assuming the same iron content regardless of the impurity concentration, the liquid combustion time and the time to peak temperature decrease with the impurity concentration (respectively up to 11.5 % and 23 % with 20 wt.% of SiO_2). Decreasing them while keeping the same amount of heat released is interesting for a practical burner. First, it limits evaporation and thus powder losses. Second, it decreases the tendency for micro-explosions, also leading to mass losses. Third, NO emissions are reduced, even though they do not represent a major problem in iron particle combustion.

After melting, the configuration taken by the liquid phases influences the combustion time and evaporation. If an impurity or a complex oxide shell forms, the liquid combustion time increases if the particle keeps burning in an external-diffusion-limited regime and more importantly Fe and FeO evaporation is limited.

The use of impure iron sources also brings challenges. First, oxide impurities represent a dead weight. For the same volumetric flow of powder injected inside a burner, the power produced decreases. As the impurity content varies considerably among impure iron sources, this implies designing burners able to adapt their power range and work with a high variability of powder composition. Second, this work highlights the potential creation of a complex oxide phase resulting from the liquid-state interactions between liquid iron oxide and the melted impurity. Even though its formation barely impacts the temperature evolution, this could prevent further oxidation to Fe_3O_4 or Fe_2O_3 and a proper reduction of Si-containing or Mn-containing complex phases. Subsequently, this would prevent both a complete energy release during the combustion, decreasing the efficiency of the closed metal-fuel cycle, and also impact the circularity of the powder if it cannot be reduced back to its initial state.

Among the four non-volatile oxide impurities studied, none of them appeared to be avoidable when working with impure iron powder. Even though they have to be tested experimentally, this is a good sign that unused impure iron sources could be utilized in the MeCRE.

Further experimental studies involving microstructure analysis are required to better understand whether a complex phase is created during the combustion and how it impacts the reduction process. Experiments could also help to better understand the configuration adopted by the phases throughout the combustion process. Building an experimental database about the temperature evolution and combustion time is crucial to validate the predictions of the current model. In particular, the impact of impurities on the transition between the external- and internal-diffusion-limited regimes should be investigated. This would require determining the evolution with temperature of the internal oxygen diffusion coefficients within liquid oxide impurities.

CRediT authorship contribution statement

Z. Bruyr: Writing – original draft, Visualization, Software, Resources, Methodology, Investigation, Funding acquisition, Conceptualization. **L. Choisez:** Writing – review & editing, Supervision, Resources, Investigation, Conceptualization. **L.C. Thijs:** Writing – review & editing, Software, Methodology. **X.C. Mi:** Writing – review & editing, Software, Methodology. **P.J. Jacques:** Supervision, Resources, Methodology. **F. Halter:** Writing – review & editing, Supervision. **F. Contino:** Writing – review & editing, Supervision, Resources, Funding acquisition, Conceptualization.

Declaration of competing interest

The authors declare the following financial interests/personal relationships which may be considered potential competing interests:

This work has received funding from the Fonds De La Recherche Scientifique - FNRS. ZB acknowledges financial support through F.R.S.-FNRS doctoral mandate. LC acknowledges financial support through F.R.S.-FNRS chargée de recherche mandate (ID40011141).

Acknowledgements

The authors acknowledge Dr. Christian Chauveau for the fruitful discussions on the parametric approach methodology. This work has received funding from the Fonds De La Recherche Scientifique - FNRS. ZB acknowledges financial support through F.R.S.-FNRS doctoral mandate. LC acknowledges financial support through F.R.S.-FNRS chargée de recherche mandate (ID40011141).

Appendix A. Supplementary data

Supplementary data for this article can be found online at doi:10.1016/j.fuel.2025.137277.

Data availability

Data will be made available upon request.

References

[1] Calcaterra M, Reis L, Fragkos P, Briera T, De Boer HS, Egli F, Emmerling J, Iyer G, Mittal S, Polzin F, Sanders M, Schmidt T, Serebriakova A, Steffen B, van de Ven D-J, Vuuren D, Waidelich P, Tavoni M. Reducing the cost of capital to finance the energy transition in developing countries. Nature Energy 2024 Sep;1–11.

[2] Clarke L, Wei Y-M, Navarro ADLV, Garg A, Hahmann AN, Khennas S, Azevedo IML, Löschel A, Singh AK, Steg L, Strbac G, Wada K. Energy systems. In Shukla PR, Skea J, Slade R, Al Khourdajie A, van Diemen R, McCollum D, Pathak M, Some S, Vyas P, Fradera R, Belkacemi M, Hasija A, Lisboa G, Luz S, Malley J, editors. Climate change 2022: mitigation of climate change. Contribution of working group III to the sixth assessment report of the Intergovernmental Panel on Climate Change. Cambridge, UK and New York, NY, USA: Cambridge University Press; 2022.

[3] Bergthorson JM, Goroshin S, Soo MJ, Julien P, Palecka J, Frost DL, Jarvis DJ. Direct combustion of recyclable metal fuels for zero-carbon heat and power. Appl Energy 2015;160:368–82. [Online]. Available: https://www.sciencedirect.com/science/article/pii/S0306261915011071.

[4] Choisez L, Van Ende M-A, Bruyr Z, Contino F, Jacques PJ. Influence of impurities on the use of Fe-based powder as sustainable fuel. Philos Trans R Soc A Math Phys Eng Sci 2024;382(2284):20230236. [Online]. Available: https://royalsocietypublishing.org/doi/abs/10.1098/rsta.2023.0236.

[5] Huang J, Li S, Sanned D, Xu L, Xu S, Wang Q, Stiti M, Qian Y, Cai W, Berrocal E, Richter M, Aldén M, Li Z. A detailed study on the micro-explosion of burning iron particles in hot oxidizing environments. Combustion Flame 2022;238:111755. [Online]. Available: https://www.sciencedirect.com/science/article/pii/S0010218021004983.

[6] Poletaev NI, Khlebnikova MY. Combustion of iron particles suspension in laminar premixed and diffusion flames. Combust Sci Technol 2022;194(7):1356–77. https://doi.org/10.1080/00102202.2020.1812588.

[7] Li S, Sanned D, Huang J, Berrocal E, Cai W, Aldén M, Richter M, Li Z. Stereoscopic high-speed imaging of iron microexplosions and nanoparticle-release. Optics Express 2021 Oct;29.

[8] Peng F, Kong C, Liu H, Mi X, Xu S, Liu Y, Cai W. Ignition and combustion of a single iron particle with impurities in hot post-flame gas flow. Combustion Flame 2024;265:113509. [Online]. Available: https://www.sciencedirect.com/science/article/pii/S0010218024002177.

[9] Soo M, Mi X, Goroshin S, Higgins A, Bergthorson J. Combustion of particles, agglomerates, and suspensions –a basic thermophysical analysis. Combustion Flame 2018 Mar;192.

[10] Mi X, Fujinawa A, Bergthorson JM. A quantitative analysis of the ignition characteristics of fine iron particles. Combustion Flame 2022;240:112011. [Online]. Available: https://www.sciencedirect.com/science/article/pii/S001021802200030X.

[11] Thijs LC, van Gool CEAG, Ramaekers WJS, van Oijen JA, de Goey LPH. Resolved simulations of single iron particle combustion and the release of nano-particles. Proc Combust Inst 2022. [Online]. Available: https://www.sciencedirect.com/science/article/pii/S1540748922000682.

[12] Ning D, Shoshin Y, van Stiphout M, van Oijen J, Finotello G, de Goey P. Temperature and phase transitions of laser-ignited single iron particle. Combustion Flame 2022;236:111801. [Online]. Available: https://www.sciencedirect.com/science/article/pii/S0010218021005447.

[13] Ning D, Shoshin Y, van Oijen JA, Finotello G, de Goey LPH. Burn time and combustion regime of laser-ignited single iron particle. Combustion Flame 2021;230:111424. [Online]. Available: https://www.sciencedirect.com/science/article/pii/S0010218021001607.

[14] Thijs LC, van Gool CEAG, Ramaekers WJS, Kuerten JGM, van Oijen JA, de Goey LPH. Improvement of heat- and mass transfer modeling for single iron particles combustion using resolved simulations. Combust Sci Technol 2024;196(4):572–88. https://doi.org/10.1080/00102202.2022.2089030

[15] Thijs LC, Kritikos EM, Giusti A, Ramaekers G, van Oijen JA, de Goey P, Mi X. On the surface chemisorption of oxidizing fine iron particles: insights gained from molecular dynamics simulations. Combustion Flame 2023;254:112871. [Online]. Available: https://www.sciencedirect.com/science/article/pii/S0010218023002523.

[16] Fujinawa A, Thijs LC, Jean-Philyppe J, Panahi A, Chang D, Schiemann M, Levendis YA, Bergthorson JM, Mi X. Combustion behavior of single iron particles, Part II: a Theoretical Analysis Based on A Zero-dimensional Model. Appl Energy Combust Sci 2023;14:100145. [Online]. Available: https://www.sciencedirect.com/science/article/pii/S2666352X23000341.

[17] Thijs LC, Van Ende M-A, van Oijen JA, de Goey P, Mi X. A numerical study of internal transport in oxidizing liquid core–shell iron particles. Combustion Flame 2025;271:113826. [Online]. Available: https://www.sciencedirect.com/science/article/pii/S0010218024005352.

[18] Mich J, da Silva AK, Ning D, Li T, Raabe D, Böhm B, Dreizler A, Hasse C, Scholtissek A. Modeling the oxidation of iron microparticles during the reactive cooling phase. Proc Combust Inst 2024;40(1):105538. [Online]. Available: https://www.sciencedirect.com/science/article/pii/S1540748924003468.

[19] Panahi A, Chang D, Schiemann M, Fujinawa A, Mi X, Bergthorson JM, Levendis YA. Combustion behavior of single iron particles–Part I: an Experimental Study in A Drop-tube Furnace Under High Heating Rates and High Temperatures. Appl Energy Combust Sci 2022. 100097. [Online]. Available: https://www.sciencedirect.com/science/article/pii/S2666352X22000401.

[20] Li T, Nguyen B-D, Gao Y, Ning D, Böhm B, Scholtissek A, van Duin ACT, Hasse C, Dreizler A. Critical nanoparticle formation in iron combustion: single particle experiments with in-situ multi-parameter diagnostics aided by multi-scale simulations, arXiv preprint 2024 arXiv:2412.08736.

[21] Nguyen B-D, Scholtissek A, Li T, Ning D, Stein OT, Dreizler A, Hasse C. Nanoparticle formation in the boundary layer of burning iron microparticles: modeling and simulation. Chem Eng J 2025;507:160039. [Online]. Available: https://www.sciencedirect.com/science/article/pii/S1385894725008381.

[22] Tóth P, Ögren Y, Sepman A, Gren P, Wiinikka H. Combustion behavior of pulverized sponge iron as a recyclable electrofuel. Powder Technol 2020;373:210–9. [Online]. Available: https://www.sciencedirect.com/science/article/pii/S0032591020304526.

[23] Choisez L, van Rooij NE, Hessels CJM, da Silva AK, Filho IRS, Ma Y, de Goey P, Springer H, Raabe D. Phase transformations and microstructure evolution during combustion of iron powder. Acta Mater 2022;239:118261. [Online]. Available: https://www.sciencedirect.com/science/article/pii/S1359645422006413.

[24] Li T, Heck F, Reinauer F, Böhm B, Dreizler A. Visualizing particle melting and nanoparticle formation during single iron particle oxidation with multi-parameter optical diagnostics. Combustion Flame 2022;245:112357. [Online]. Available: https://www.sciencedirect.com/science/article/pii/S0010218022003728.

[25] Wiinikka H, Vikström T, Wennebro J, Toth P, Sepman A. Pulverized sponge iron, a zero-carbon and clean substitute for fossil coal in energy applications. Energy Fuels 2018 Aug;32.

[26] Prasidha W, Baigmohammadi M, Shoshin Y, de Goey P. Towards an efficient metal energy carrier for zero–emission heating and power: iron powder combustion. Combustion Flame 2024;268:113655. [Online]. Available: https://www.sciencedirect.com/science/article/pii/S001021802400364X.

[27] Cen L, Lyu Z, Qian Y, Li Z, Lu X. In-situ light extinction nano-oxide volume fraction measurements during single iron particle combustion. Proc Combust Inst 2024;40(1):105305. [Online]. Available: https://www.sciencedirect.com/science/article/pii/S1540748924001159.

[28] Chen R, Thijs LC, Hansen BB, Lin W, Wu H, Glarborg P, Fujinawa A, Mi X. Combustion of micron-sized iron particles in a drop tube reactor. Fuel 2025;383:133814. [Online]. Available: https://www.sciencedirect.com/science/article/pii/S0016236124029636.

[29] Chang D, Thijs LC, Panahi A, Mi X, Bergthorson JM, Levendis YA. Effects of oxygen concentration on nanoparticle formation during combustion of iron powders. Fuel 2025;397:135366. [Online]. Available: https://www.sciencedirect.com/science/article/pii/S0016236125010919.

[30] Ning D, Shoshin Y, van Oijen JA, Finotello G, de Goey L. Critical temperature for nanoparticle cloud formation during combustion of single micron-sized iron particle. Combustion Flame 2022;244:112296. [Online]. Available: https://www.sciencedirect.com/science/article/pii/S001021802200311X.

[31] Ning D, Shoshin Y, van Oijen J, Finotello G, de Goey P. Size evolution during laser-ignited single iron particle combustion. Proc Combust Inst 2022. [Online]. Available: https://www.sciencedirect.com/science/article/pii/S1540748922000724.

[32] Zeldvich YB. The oxidation of nitrogen in combustion and explosions. Acta Physicochimica 1946;21:577.

[33] Ravi A, Hazenberg T, Thijs LC, van Oijen JA, de Goey LPH. Nitrogen oxide formation mechanism in iron dust flames. Proc Combust Inst 2024;40(1):105611. [Online]. Available: https://www.sciencedirect.com/science/article/pii/S1540748902400419X.

[34] Baigmohammadi M, Prasidha W, Stevens NC, Shoshyn YL, Spee T, de Goey P. Towards utilization of iron powders for heating and power. Appl Energy Combust Sci 2023;13:100116. [Online]. Available: https://www.sciencedirect.com/science/article/pii/S2666352X23000055.

[35] Stevens NC, Prasidha W, Deen NG, Meeuwsen L, Baigmohammadi M, Shoshin Y, de Goey LPH, Finotello G. Cyclic reduction of combusted iron powder: a study on the material properties and conversion reaction in the iron fuel cycle. Powder Technol 2024;441:119786. [Online]. Available: https://www.sciencedirect.com/science/article/pii/S0032591024004297.

[36] Cheraghi A, Yoozbashizadeh H, Safarian J. Gaseous reduction of manganese ores: a review and theoretical insight. Min Process Extr Metall Rev 2019 Aug.

[37] Hazenberg T, van Oijen JA. Structures and burning velocities of flames in iron aerosols. Proc Combust Inst 2021;38(3):4383–90. [Online]. Available: https://www.sciencedirect.com/science/article/pii/S1540748920304909.

[38] Shishin D, Prostakova V, Jak E, Decterov S. Critical assessment and thermodynamic modeling of the Al-Fe-O system. Metall Mater Trans B 2015 Nov;47.

[39] Luo Y-H, Zhu D-Q, Zhou X, Shi B, Zhang F. Coproduction of DRI powder and semi-coke from siderite ore and low rank coal by excessive coal-based direct reduction in rotary kiln. ISIJ Int 2015 Nov;56.

[40] Shultz R, Muan ARNULF. Phase equilibria in the system Mno-“FeO”-ZrO2-SiO2. J Am Ceram Soc 2006 Jun;54:504–10.

[41] Eustathopoulos N. Wetting by liquid metals—application in materials processing: the contribution of the Grenoble group. Metals 2015;5(1):350–70. [Online]. Available: https://www.mdpi.com/2075-4701/5/1/350.

[42] Ning D, Li T, Mich J, Scholtissek A, Böhm B, Dreizler A. Multi-stage oxidation of iron particles in a flame-generated hot laminar flow. Combustion Flame 2023;256:112950. [Online]. Available: https://www.sciencedirect.com/science/article/pii/S0010218023003267.

[43] Niu Y, Tan H, Ma L, Pourkashanian M, Liu Z, Liu Y, Wang X, Liu H, Xu T. Slagging characteristics on the superheaters of a 12 MW biomass-fired boiler. Energy Fuels 2010;24(9):5222–7. https://doi.org/10.1021/ef1008055

[44] Thijs L, Kritikos E, Giusti A, Van Ende M-A, Duin A, Mi X. Effect of Fe–O ReaxFF on liquid iron oxide properties derived from reactive molecular dynamics. J Phys Chem A 2023 Nov;127.

[45] Heuer AH. Oxygen and aluminum diffusion in α-Al2O3: how much do we really understand? J Eur Ceram Soc 2008, developments in Ceramic Science and Engineering: the last 50 years. A meeting in celebration of Professor Sir Richard Brook’s 70th Birthday. 28(7):1495–507. [Online]. Available: https://www.sciencedirect.com/science/article/pii/S0955221907006097.

[46] Sperling A, Deutschmann MP, Ning D, Spielmann J, Li T, Kramm UI, Nirschl H, Böhm B, Dreizler A. Oxidation progress and inner structure during single micron-sized iron particles combustion in a hot oxidizing atmosphere. Fuel 2025;381:133147. [Online]. Available: https://www.sciencedirect.com/science/article/pii/S0016236124022968.

[47] Deutschmann MP, Sperling A, Covini E, Böhm B, Dreizler A, Nirschl H. Single iron particle combustion - a morphology study of partially oxidized iron particles. Powder Technol 2024;445:120102. [Online]. Available: https://www.sciencedirect.com/science/article/pii/S0032591024007460.

[48] Bruyr Z, Hameete J, Choisez L, Halter F, Contino F. Observation of an unmixed particle surface during single-particle experiments of iron combustion. Fuel 2025;395:135261. [Online]. Available: https://www.sciencedirect.com/science/article/pii/S001623612500986X.

[49] Hasegawa M. Chapter 3.3 - Ellingham diagram. In Seetharaman S, editor. Treatise on process metallurgy. Boston: Elsevier; 2014. pp. 507–16. [Online]. Available: https://www.sciencedirect.com/science/article/pii/B9780080969862000321.

[50] El-Geassy A-HA, Nasr MI, Omar AA, Mousa E-SA. Influence of SiO2 and/or MnO2 on the reduction behaviour and structure changes of Fe2O3 compacts with CO gas. ISIJ Int 2008;48(10):1359–67.

[51] Wang HT, Sohn HY. Effect of CaO and SiO2 on swelling and iron whisker formation during reduction of iron oxide compact. Ironmak Steelmak 2011;38(6):447–52. https://doi.org/10.1179/1743281211Y.0000000022

[52] Guo H, Jiang X, Shen F, Zheng H, Gao Q, Zhang X. Influence of SiO2 on the compressive strength and reduction-melting of pellets. Metals 2019;9(8). [Online]. Available: https://www.mdpi.com/2075-4701/9/8/852.

[53] Halim KSA, Bahgat M, El-Kelesh HA, Nasr MI. Metallic iron whisker formation and growth during iron oxide reduction: basicity effect. Ironmak Steelmak 2009;36(8):631–40. https://doi.org/10.1179/174328109X463020

[54] Kim W-H, Lee Y-S, Suh I-K, Min D-J. Influence of CaO and SiO2 on the reducibility of wüstite using H2 and CO gas. ISIJ Int 2012;52(8):1463–71.

[55] Bahgat M, Halim KSA, Nasr MI, El-Geassy AA. Morphological changes accompanying gaseous reduction of SiO2 doped wüstite compacts. Ironmak Steelmak 2008;35(3):205–12. https://doi.org/10.1179/174328107X155259

[56] Ono-Nakazato H, Okada K, Usui T. Effects of slag content and composition on the reducibility of iron oxide including CaO-SiO2-FeO slag. ISIJ Int 2005;45(4):569–73.

[57] Shigematsu N, Iwai H. Effect of the addition of SiO2 and SiO2-CaO on the reduction of dense wustite at high temperatures. Tetsu-To-Hagané 1993;79(8):920–6.

[58] Patterer L, Mayer EB, Mráz S, Pöllmann PJ, Hans M, Primetzhofer D, Souza Filho IR, Springer HJ, Schneider JM. Effect of Si on the hydrogen-based direct reduction of Fe2O3 studied by XPS of sputter-deposited thin-film model systems. Scripta Materialia 2023;233:115515. [Online]. Available: https://www.sciencedirect.com/science/article/pii/S1359646223002397.

[59] Nakiboglu F, John DHS, Hayes PC. The gaseous reduction of solid calciowustites in CO/CO_2 and H_2/H_2O gas mixtures. Metallurgical Transactions B 1986;17:375–81.

[60] Shigematsu N, Iwai H. Effect of the addition of Al2O3 and Al2O3-Ca0 on the reduction of dense wustite with H2. Tetsu-To-Hagané 1987;73(16):2243–50.

[61] Kapelyushin Y, Xing X, Zhang J, Jeong S, Sasaki Y, Ostrovski O. Effect of alumina on the gaseous reduction of magnetite in CO/CO_2 gas mixtures. Metall Mater Trans B 2015;46:1175–85.

[62] Paananen T, Heinänen K, Härkki J. Degradation of iron oxide caused by alumina during reduction from magnetite. ISIJ Int 2003;43(5):597–605.

[63] Kapelyushin Y, Sasaki Y, Zhang J, Jeong S, Ostrovski O. Formation of a network structure in the gaseous reduction of magnetite doped with alumina. Metall Mater Trans B 2017;48:889–99.

[64] Sastri MVC, Viswanath RP, Viswanathan B. Studies on the reduction of iron oxide with hydrogen. Int J Hydrogen Energy 1982;7(12):951–5. [Online]. Available: https://www.sciencedirect.com/science/article/pii/036031998290163X.

[65] El-Geassy A-HA, Nasr MI, Omar AA, Mousa E-SA. Reduction kinetics and catastrophic swelling of MnO2-doped Fe2O3 compacts with CO at 1073–1373 K. ISIJ Int 2007;47(3):377–85.

[66] Go KS, Son SR, Kim SD. Reaction kinetics of reduction and oxidation of metal oxides for hydrogen production. Int J Hydrogen Energy 2008;33(21):5986–95. [Online]. Available: https://www.sciencedirect.com/science/article/pii/S0360319908005843.